NANO LETTERS

pubs.acs.org/NanoLett Letter

Broadening Near-Field Emission for Performance Enhancement in Thermophotovoltaics

Georgia T. Papadakis, Siddharth Buddhiraju, Zhexin Zhao, Bo Zhao, and Shanhui Fan*

Cite This: *Nano Lett.* 2020, 20, 1654−1661 Read Online

ACCESS | Metrics & More | Article Recommendations

ABSTRACT: The conventional notion for achieving high efficiency in thermophotovoltaics (TPVs) is to use a monochromatic emission at a photon energy corresponding to the band gap of the cell. Here, we prove theoretically that such a notion is only accurate under idealized conditions and further show that, when nonradiative recombination is taken into account, efficiency improvement can be achieved by broadening the emission spectrum, due to an enhancement in the open-circuit voltage. Broadening the emission spectrum also improves the electrical power density, by increasing the short-circuit current. Hence, broadening the emission spectrum can simultaneously improve the efficiency and power density of practical TPV systems. To illustrate these findings, we focus on surface polariton-mediated near-field TPVs. We propose a versatile design strategy for broadening the emission spectrum via stacking of multiple plasmonic thin film layers. As an example, we consider a realistic ITO/InAs TPV and predict a conversion efficiency of 50% simultaneously with a power density of nearly 80 W/cm^2 at a 1300 K emitter temperature. The performance of our proposed system far exceeds previous works in similar systems using a single plasmonic layer emitter.

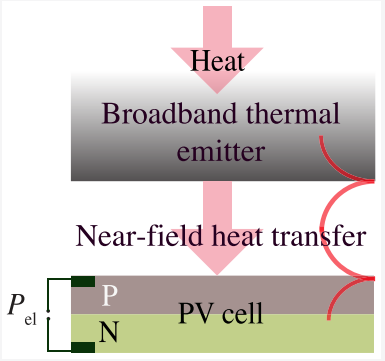

KEYWORDS: *thermophotovoltaic systems, thermal emission, photon recycling, nonradiative recombination, near-field*

A thermophotovoltaic (TPV) system is a solid-state renewable energy approach that is of potential importance for a number of applications including solar energy harvesting and waste heat recovery. In these systems, a photovoltaic (PV) cell is separated from a thermal emitter by a vacuum gap. The PV cell converts the thermal radiation from the emitter into electricity. Since far-field thermal radiation is fundamentally limited in its power density by the blackbody limit, a significant portion of the literature is exploring near-field TPV systems.[1−14] In these systems, by reducing the spacing between the PV cell and the thermal emitter to be smaller than the relevant thermal wavelength, the power density can far exceed that in the far-field system. Initial experiments realized vacuum gap spacings on the order of a micron and utilized low-band-gap materials for the PV, namely, InAs[15] and InGaAs.[16] Most recently, a TPV system with a vacuum gap of 60 nm that separates a flat emitter from an InAsSb/InAsSbP PV cell, with surface areas on the order of few hundreds of μm^2, has been realized and measured.[17]

In standard analysis for TPV systems, assuming an idealized PV cell without nonradiative recombination, it is known that the efficiency of the TPV maximizes to the Carnot efficiency limit when the thermal exchange spectrum between the emitter and the PV cell has a narrow band, located at the band gap of the PV cell.[2,18] Motivated by this analysis, significant efforts have been devoted to develop near-field TPV systems where the emitters support surface plasmon[2,4,5,19−22] or phonon[1] polaritons, and hence, the thermal exchange spectrum between the emitter and the PV cell is narrow-banded.[2,7,10] Recently, the effects of the size of the bandwidth of emission on the TPV efficiency were investigated theoretically;[11] however, this analysis focused primarily on ideal systems without nonradiative recombination.

In this paper, we provide a theoretical analysis of a TPV system, where the PV cell has significant nonradiative recombination, as is typical for most PV cells assumed in previous analysis of near-field TPV systems. We show that, in the presence of significant nonradiative recombination, starting from the narrow-band thermal emission limit as discussed above, the efficiency in fact *increases* as the bandwidth of the thermal exchange increases. Since in general the power density of the TPV system should increase as the bandwidth of the thermal exchange increases, our results indicate that increasing the bandwidth of the thermal exchange in fact increases *both* the efficiency and the power density of TPV systems.

Motivated by this theoretical analysis, we then focus on near-field TPVs and outline design strategies for achieving a broad-band plasmonic near-field thermal emitter by introducing a spatial gradient of the plasma frequency. We show that

Received: November 18, 2019
Revised: January 11, 2020
Published: January 24, 2020

https://dx.doi.org/10.1021/acs.nanolett.9b04762
Nano Lett. 2020, 20, 1654−1661

such a design of a broad-band near-field thermal emitter significantly increases the power density and efficiency of a TPV system simultaneously, as compared with the use of a standard plasmonic near-field emitter.

We start by considering a detailed balance analysis of a TPV system with an emitter at temperature T_H and a cell at temperature T_C.[23] The current density $J(V)$ of the PV cell is

$$J(V) = J_e - J_o e^{qV/kT_C} + R_o - R(V) \tag{1}$$

where V is the operating voltage of the cell. The first and second terms correspond, respectively, to the radiative generation and recombination of electron−hole pairs, whereas the third and fourth terms correspond to nonradiative generation and recombination, respectively. J_0 is the current arising from the thermal emission of the cell, whereas J_e arises from the absorption of the cell in the frequency range above the band gap. These are given by

$$J_{o/e} = \frac{q}{4\pi^2}\int_{\omega_g}^{\infty} \Phi(\omega) n(\omega, T_{C/H})\, d\omega \tag{2}$$

where $n(\omega, T) = (e^{\hbar\omega/kT} - 1)^{-1}$ is the Planck distribution for photons with energy $\hbar\omega$ at temperature T, ω_g is the band gap, and $\Phi(\omega)$ is the normalized emission spectrum. In eq 2, we considered the case where radiative exchange occurs exclusively between the cell and the emitter; i.e., there is no radiation leakage to the environment. Based on the standard treatment with fluctuational electrodynamics,[24−28] $\Phi(\omega)$ is given by

$$\Phi(\omega) = \int_0^{\infty} \xi(\omega, \beta)\beta\, d\beta \tag{3}$$

where $\xi(\omega, \beta)$ is the probability, summed over the two polarizations, for a photon with frequency ω, and in-plane wavenumber β, to be transmitted through the vacuum gap.

The efficiency of a TPV system is defined as the ratio $\eta = (P_{el}/P_{phot}) \times 100\%$, where $P_{el} = J(V) \times V$ is the extracted electrical power density and P_{phot} is the photonic heat exchange between the emitter and the cell, given by $P_{phot} = P_{\omega<\omega_g} + P_{\omega>\omega_g}$, where the terms $P_{\omega<\omega_g}$ and $P_{\omega>\omega_g}$ correspond, respectively, to heat exchange below and above the band gap. These are given by $P_{\omega<\omega_g} = Q_{e,\omega<\omega_g} - Q_{o,\omega<\omega_g}$ and $P_{\omega>\omega_g} = Q_{e,\omega>\omega_g} - Q_{o,\omega>\omega_g} e^{qV/kT_C}$, where

$$Q_{o/e,\omega<\omega_g} = \frac{1}{4\pi^2}\int_0^{\omega_g} \hbar\omega\Phi(\omega) n(\omega, T_{C/H})\, d\omega \tag{4}$$

and

$$Q_{o/e,\omega>\omega_g} = \frac{1}{4\pi^2}\int_0^{\omega_g} \hbar\omega\Phi(\omega) n(\omega, T_{C/H})\, d\omega \tag{5}$$

The term $P_{\omega<\omega_g}$ corresponds to below-band-gap absorption of the cell and becomes particularly important for PV cells made of polar semiconductors.[29]

In the absence of an applied bias in the PV cell, the nonradiative generation and recombination currents in eq 1 are balanced; hence, the short-circuit current ($J_{sc} = J(V = 0)$) is

$$J_{sc} = J_e - J_o \tag{6}$$

Following Shockley−Queisser analysis,[23] we first use a simple model that facilitates analytic derivation by assuming $R(V) = R_o e^{qV/kT_C}$. Then, based on eq 1, the open-circuit voltage ($J(V_{oc}) = 0$) becomes

$$V_{oc} = \frac{kT_C}{q}\ln\left[\frac{J_e + R_o}{J_o + R_o}\right] \tag{7}$$

It is generally desirable to increase both J_{sc} and V_{oc}, which increases the power density. Below, we show that increasing V_{oc} also increases the efficiency.

Assuming a normalized emission spectrum that is nonzero only within the frequency range $[\omega_g, \omega_g + \delta\omega]$ and ignoring below-band-gap heat exchange ($P_{\omega<\omega_g} = 0$), the upper limit of integration in eqs 2 and 5 becomes $\omega_g + \delta\omega$. By further assuming that $\hbar\omega_g \gg kT_H$, $\hbar\delta\omega \ll kT_C$, and $\Phi(\omega)$ is slowly varying within the range of $[\omega_g, \omega_g + \delta\omega]$, to the second order of $\delta\omega$, the integrations in eqs 2 and 5 can be evaluated to give

$$J_{o/e} = \frac{q}{4\pi^2}\delta\omega\Phi(\omega_g) e^{-\hbar\omega_g/kT_{C/H}}\left[1 - \frac{\hbar\delta\omega}{2kT_{C/H}}\right] \tag{8}$$

and

$$Q_{o/e,\omega>\omega_g} = J_{o/e}\frac{\hbar}{q}\left(\omega_g + \frac{\delta\omega}{2}\right) \tag{9}$$

Then, the efficiency approaches

$$\eta \approx \frac{qV}{\hbar(\omega_g + \delta\omega/2)} \tag{10}$$

suggesting that the maximum efficiency corresponds to the open-circuit voltage, V_{oc}.

We now consider two regimes, the radiative regime, where radiative recombination dominates, i.e., $R_0 \ll J_0$, and the nonradiative region, where nonradiative recombination dominates, i.e., $R_0 \gg J_0$. In the radiative regime, from eq 7 and eq 8, we obtain

$$V_{oc} = \frac{\hbar\omega_g}{q}(1 - T_C/T_H) + \frac{kT_C}{q}\ln\left[\frac{T_C(2kT_H - \hbar\delta\omega)}{T_H(2kT_C - \hbar\delta\omega)}\right] \tag{11}$$

Correspondingly, for a monochromatic spectrum, i.e., for $\delta\omega \to 0$, eqs 10 and 11 yield $\eta = 1 - T_C/T_H$.[30−32] This is the Carnot thermodynamic efficiency limit of a heat engine. When $\delta\omega$ increases from 0, the efficiency decreases, as can be seen in eq 10.

In contrast to the radiative regime, however, many semiconducting materials used in TPV systems are subject to substantial nonradiative recombination. For these semiconductors, the nonradiative regime is more relevant. In this case, it is easy to see from eqs 6 and 8 that the short-circuit current, J_{sc}, increases linearly with $\delta\omega$. In the nonradiative limit, the J_0 term in the denominator of eq 7 becomes irrelevant and V_{oc} can be written as

$$V_{oc} = \frac{kT_C}{q}\ln\left[\frac{\delta\omega}{R_o'} + 1\right] \tag{12}$$

where $R_o' = (4\pi^2 R_0 e^{\hbar\omega_g/kT_H})/(q\Phi(\omega_g))$. Therefore, the open-circuit voltage increases with the bandwidth $\delta\omega$. Since both the short-circuit current and open-circuit voltage increase with bandwidth, we expect that the electrical power density also increases with the exchange spectrum bandwidth. Importantly, the same can be said for the efficiency. Particularly, eqs 10 and 12 yield

https://dx.doi.org/10.1021/acs.nanolett.9b04762
Nano Lett. 2020, 20, 1654−1661

$$\eta \approx \frac{kT_C}{\hbar(\omega_g + \delta\omega/2)} \ln\left[\frac{\delta\omega}{R_o'} + 1\right] \tag{13}$$

One can show that η is an increasing function of $\delta\omega$ as long as $\delta\omega \ll \omega_g$. In this limit, therefore, we have shown here that the efficiency and power density of a TPV system can be increased simultaneously by broadening the bandwidth of the normalized emission spectrum. So far, our treatment pertains to both far-field and near-field TPVs. In what follows, we focus on near-field TPVs due to significantly better performance in terms of both power density and efficiency, compared to far-field TPVs.[2,10,22]

Motivated by the discussion above, below, we outline a practical design strategy for broadening the normalized emission spectrum $\Phi(\omega)$ in an exemplary near-field TPV system. The system consists of an InAs cell facing a plasmonic indium tin oxide (ITO) emitter, as shown in the inset of Figure 1a. As a heat source, we consider a tungsten back-side reflector that uniformly spreads thermal energy to the ITO surface area.

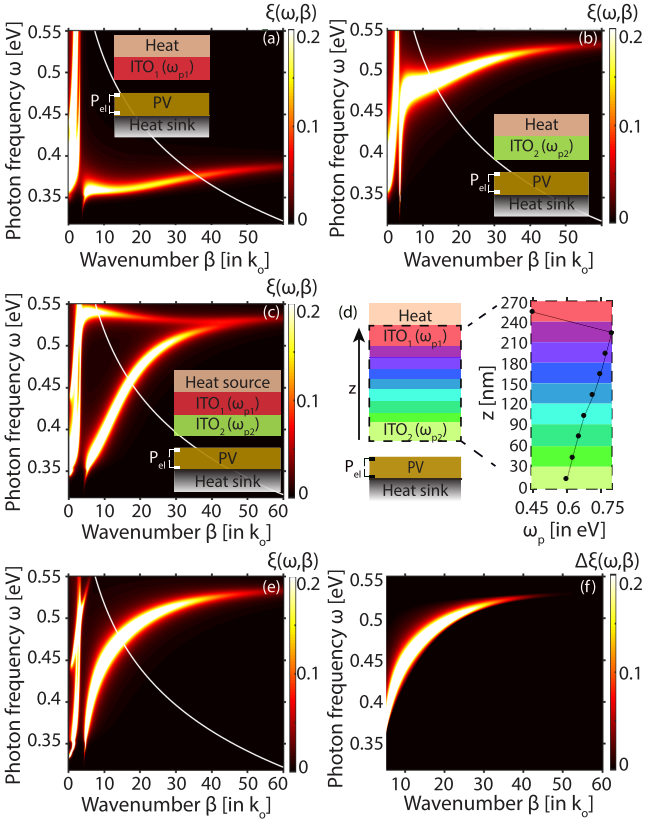

Figure 1. Photon transmission probability $\xi(\omega, \beta)$ for (a) a conventional near-field TPV consisting of a 400 nm InAs cell and a single-layer 30 nm ITO emitter with $\omega_{p1} = 0.44$ eV, at a vacuum gap distance of $d = 10$ nm. (b) Same as part a but for $\omega_{p2} = 0.6$ eV. (c) Bilayer emitter case with $\omega_{p1} = 0.44$ eV and $\omega_{p2} = 0.6$ eV. The white curve in parts a–c corresponds to the Planck distribution $n(\omega, T_H = 1300\ \text{K})$. (d) The left side shows a schematic of a design strategy for further enhancing heat transfer by inserting a plasmonic heterostructure between the top and bottom emitter layers in part c. The plasma frequency distribution $\omega_p(z)$ in the heterostructure is shown on the right. (e) Photon transmission probability for the schematic of panel d and (f) its difference from the photon transmission probability of panel c. The x-axis of the contour plots is normalized to the free-space wavenumber $k_0 = \omega/c$.

To ensure recycling of low-energy photons, a perfect electric conductor layer is placed at the back side of the cell (heat sink in the inset of Figure 1a).[33] This motif has been previously shown to achieve the largest reported combination of efficiency and power density in simulations.[22] Similar to ref 22, we consider a separation distance of $d = 10$ nm between the emitter and the cell. The optical properties of InAs as well as tungsten have been obtained from ref 34.

We describe the permittivity of ITO with the Drude model $\epsilon(\omega) = \epsilon_\infty(1 - \omega_p^2/(\omega^2 + i\omega\gamma))$, where $\epsilon_\infty = 4$ and ω_p and γ are the plasma frequency and damping rate of ITO, respectively. The damping rate of ITO lies in the range $\gamma = 0.1-0.15$ eV.[5,22,35,36] In the numerical results that follow (Figures 2–4), we consider $\gamma = 0.1$ eV. Nevertheless, in order to clearly illustrate the physics of the proposed scheme of broadening the bandwidth of the normalized emission spectrum, in Figure 1, we reduce the damping rate of ITO by 1 order of magnitude ($\gamma' = 0.01$ eV) and discuss in what follows the photon transmission probability, $\xi(\omega, \beta)$. As seen in Figure 1a, where the plasma frequency of the ITO emitter is set to $\omega_{p1} = 0.44$ eV, the heat exchange is relatively narrow in bandwidth. Increasing the plasma frequency to $\omega_{p2} = 0.6$ eV blueshifts the frequency range where heat transfer is maximized; nevertheless, the bandwidth remains narrow, as shown in Figure 1b. In order to broaden the bandwidth, we consider a bilayer emitter composed of the two previous layers with plasma frequencies ω_{p1} and ω_{p2}, where the layer with the larger plasma frequency (ω_{p2}) is placed closer to the vacuum gap, as can be seen in the inset of Figure 1c. The bandwidth of the heat exchange in this bilayer emitter case has considerably increased, which can be understood as follows: at large in-plane wavenumbers, $\beta \to \infty$, evanescent modes that tunnel from the bilayer emitter to the cell have little penetration into the top layer (ω_{p1}); therefore, only the layer closest to the vacuum gap contributes to heat transfer, for which heat transfer becomes prominent at high frequencies approaching ω_{p2}. Analogously, at small wavenumbers, $\beta \to 0$, the field expands across the whole depth of the bilayer emitter, thereby allowing for a considerable amount of heat exchange to occur via modes supported by the top layer (red layer in Figure 1c). Hence, the point of maximum heat transfer (maximum $\xi(\omega, \beta)$) redshifts toward ω_{p1} as β decreases. The heat exchange bandwidth in Figure 1c is nearly $[\omega_{p1}, \omega_{p2}]$ and can be engineered on demand through the selection of ω_{p1}, ω_{p2}.

Building upon the concept of the bandwidth broadening, the heat exchange between the emitter and the cell within the bandwidth $[\omega_{p1}, \omega_{p2}]$ can be further increased, which improves the TPV performance in terms of both power density and conversion efficiency, as we demonstrate below. To increase the heat transfer within the spectral region $[\omega_{p1}, \omega_{p2}]$, we insert a heterostructure composed of thin plasmonic layers in between the top (ω_{p1}) and bottom (ω_{p2}) layers, as shown in the schematic of Figure 1d, where the plasma frequency profile in this heterostructure, $\omega_p(z)$, is shown on the right. With this modification, each plasmonic film with $\omega_{p,i}$, for $i = 1, 2, \ldots$, provides additional contributions to heat transfer due to supported plasmonic modes occurring at energies lower than $\omega_{p,i}$.[37] Since the absolute wavenumber β of a plasmonic mode scales with its respective plasma frequency $\omega_{p,i}$, decreasing the plasma frequency as one approaches the vacuum gap maximizes the contribution of each layer to heat transfer. In Figure 1e, we show the photon transmission probability of the optimized structure (schematic in Figure 1d), whereas, in

https://dx.doi.org/10.1021/acs.nanolett.9b04762
Nano Lett. 2020, 20, 1654−1661

Figure 1f, we show its difference from the photon transmission probability of the bilayer emitter of Figure 1c. The bright regions in the (ω, β) plane of Figure 1f, therefore, show the additional contributions to heat transfer, enabled by the inserted plasmonic heterostructure. Hence, we have shown here that introducing a spatial gradient of the plasma frequency of the emitter, as shown in Figure 1d, improves heat transfer from the emitter to the cell.

The parameters of ITO considered here can be practically realized with sputtering and pulsed-laser deposition (PLD).[38−40] Using these methods, thin continuous films on the order of a few nanometers can be deposited.[41] Hence, the plasma frequency profile shown in Figure 1d is feasible experimentally, for example, through a gradual change in the doping profile of the ITO region, achieved by gradually altering the deposition conditions, e.g., carrier density, oxygen concentration and temperature,[40,42] or pressure.[43]

Assuming that one has the flexibilty to select the band gap of the semiconductor for the PV cell, the selection of the bilayer emitter's plasma frequencies, ω_{p1} and ω_{p2}, in Figure 1c, depends critically on the temperature of the emitter, T_H. The normalized emission spectra for the structures in Figure 1c and e lie largely in the interval $[\omega_{p1}, \omega_{p2}]$. The Planck distribution $n(\omega, T_H)$ at the emitter temperature T_H decreases with increasing ω and becomes negligible when $\omega \gg kT_H$, whereas the density of the states associated with heat exchange increases with frequency in a slower rate. Combining these two considerations, one should, therefore, select the plasma frequencies to be slighlty larger than $kT_H/\hbar$. Our choice of the plasma frequency ω_{p1} = 0.44 eV in Figure 1a,c is for an emitter with a temperature of T_H = 1300 K, as can be seen by the white curve which corresponds to $n(\omega, T_H = 1300\ K)$. The plasma frequency ω_{p2} = 0.6 eV in Figure 1b,c was selected in order to clearly visualize the bandwidth broadening mechanism in the low-loss limit. However, for emitter temperatures in the range of T_H = 1300 K, in what follows, we reduce ω_{p2} to 0.5 eV.

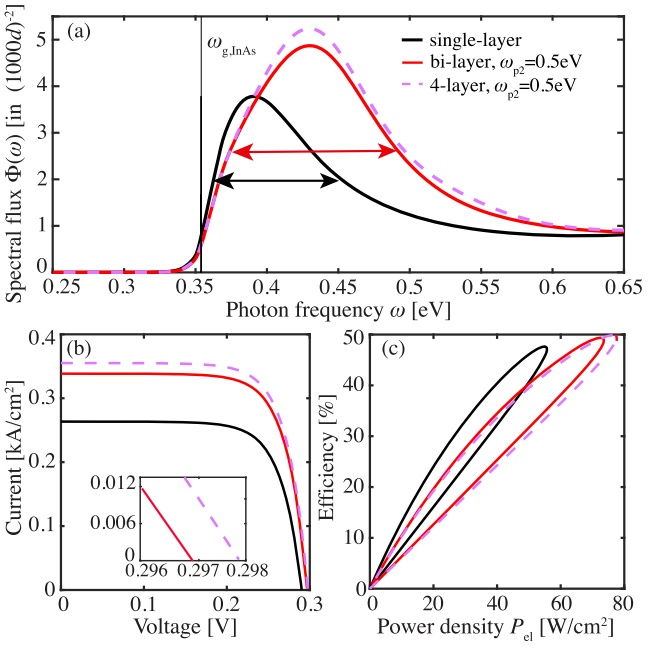

Figure 2. (a) Normalized emission spectrum, $\Phi(\omega)$, for a near-field TPV with an InAs cell and an ITO emitter. The single-layer emitter case pertains to the schematic in the inset of Figure 1a, with ω_{p1} = 0.44 eV. The bilayer case pertains to the schematic in the inset of Figure 1c for ω_{p2} = 0.5 eV. The arrows indicate the bandwidth of the corresponding normalized emission spectra. The four-layer emitter case corresponds to implementing the design strategy of Figure 1d, with the intermediate layers having ω_{p3} = 0.6 eV and ω_{p4} = 0.575 eV. (b) Current−voltage characteristics. The inset magnifies the range where the current is near-zero. The voltage at zero current is the open-circuit voltage, V_{oc}. (c) Efficiency η vs power density P_{el} showing a simultaneous increase in η and P_{el} as the number of layers increases.

We now show that the bandwidth broadening strategy as shown in Figure 1 can indeed be used to improve the performance of near-field TPV systems. As a benchmark, we consider the single-layer emitter near-field TPV displayed in the schematic of Figure 1a, for an InAs cell, and an ITO plasmonic emitter with ω_{p1} = 0.44 eV and γ = 0.1 eV. In the following results, we account for nonidealities in the materials, namely, below-band-gap absorption (as outlined in the formalism above, see eq 4) and nonradiative recombination in InAs.

Regarding nonradiative processes in InAs, the Shockley−Read−Hall (SRH) and Auger nonradiative mechanisms are dominant, and they constitute the first and second terms, respectively,[44] in

$$R(V) = \frac{pn - n_i^2}{\tau(n + p + 2n_i)} t_c + (C_p p + C_n n)(np - n_i^2) t_c. \tag{14}$$

In eq 14, t_c is the thickness of the cell, τ is the SRH lifetime, C_n and C_p are the Auger coefficients, n_i is the intrinsic carrier concentration in the cell, and n and p are the electron and hole densities, respectively. For InAs, τ = 100 nm, $C_n = C_p = 2.26 \times 10^{-27}$ cm^6/s, and $n_i = 2 \times 10^{16}$ cm^{-3}.[45] We set the thickness of the InAs cell to t_c = 400 nm (similar to Figure 1), which maximizes the power density in the presence of nonradiative recombination.[22]

We set the cell temperature at T_C = 300 K and the emitter temperature at T_H = 1300 K. In Figure 2a, we display the normalized emission spectrum $\Phi(\omega)$ for the single-layer emitter configuration with the black curve, and its bandwidth (full width at half-maximum) is shown with the black arrow. By considering the bilayer emitter, as shown in the schematic of Figure 1c, with ω_{p2} = 0.5 eV, the spectrum broadens considerably, as can be seen with the red curve and arrow in Figure 2a. In Figure 2b, we show that this bandwidth broadening indeed yields a simultaneous increase in short-circuit current and open-circuit voltage.

Next, we implement the strategy outlined in Figure 1d−f for further increasing the heat transfer, by inserting intermediate plasmonic layers in between the layers with ω_{p1} and ω_{p2}. Here, we consider two intermediate layers with ω_{p3} = 0.6 eV and ω_{p4} = 0.575 eV in the sequence displayed in Figure 1d. With these additional layers, the bandwidth of the normalized emission spectrum does not change significantly compared to the two-layer structure; however, its amplitude increases, as shown in Figure 2a. In Figure 2b, we confirm that adding these intermediate layers in the emitter structure yields indeed a further increase in short-circuit current and open-circuit voltage.

In Figure 2c, we display the efficiency, η, versus power density, P_{el}, obtained by tuning the load voltage V from 0 to V_{oc}. Increasing the number of emitter layers with respect to the single-layer emitter (black curve) simultaneously increases the

https://dx.doi.org/10.1021/acs.nanolett.9b04762
Nano Lett. 2020, 20, 1654−1661

power density and efficiency, in consistency with the increase in I_{sc} and V_{oc}, respectively, as discussed above.

In Figure 3, we study the performance of the near-field TPVs discussed in Figure 2 for a wide range of emitter temperatures

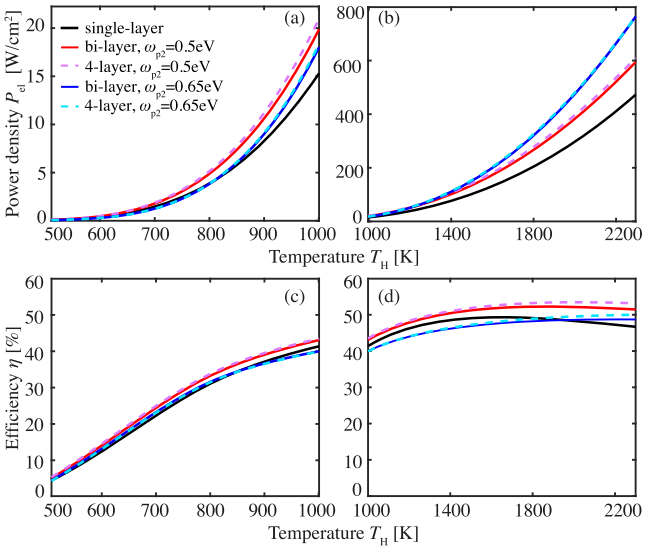

Figure 3. (a, b) Power density P_{el} and (c, b) efficiency η for the single-layer emitter case and for the bilayer emitter and four-layer cases as a function of T_H. Panels a and c correspond to the waste heat temperature range, whereas panels b and d correspond to higher emitter temperatures. The solid red and dashed pink curves correspond to a selection of ω_{p2} = 0.5 eV for optimizing performance near the waste heat temperature range, the same as that in Figure 2. The solid blue and dashed cyan curves correspond to ω_{p2} = 0.65 eV for optimizing performance at higher temperatures.

from T_H = 500 K to the melting point of ITO at T_H = 2200 K. Particularly, we show the power density (Figure 3a,b) and efficiency (Figure 3c,d) for the single-layer emitter configuration (black curves) and compare with the bilayer emitter case (red curves) for ω_{p2} = 0.5 eV, considered in Figure 2, and the corresponding four-layer emitter case (dashed pink curves). In terms of power density, the bilayer yields a significant improvement with respect to the single-layer emitter, in the temperature range T_H < 1000 K (Figure 3a), which is important for practical applications of TPVs, since it corresponds to the waste heat, low-grade temperature range where the largest portion of the energy consumed by the manufacturing sector is rejected into the environment in the form of waste heat.[22,46] We also present results where we optimize the TPV power density at higher emitter temperatures, shown in Figure 3b. In this higher temperature operation, it is important to considerably blueshift the normalized emission spectra $\Phi(\omega)$ shown in Figure 2, by increasing ω_{p2} to ω_{p2} = 0.65 eV. Therefore, for high temperatures, using a bilayer emitter with ω_{p2} = 0.65 eV (blue curves), we achieve a significantly higher power density as compared to the case with ω_{p2} = 0.5 eV, as shown in Figure 3b. Further small improvement is possible with the use of a four-layer emitter with ω_{p3} = 0.75 eV and ω_{p4} = 0.725 eV (dashed cyan curves), due to thermal emission enhancement as discussed in Figure 1d−f.

From Figure 3a,b, it can be seen that the power density increases with the number of emitter layers for both considered values of ω_{p2}. At the lower temperature of 1300 K, we achieve a maximum power density of 78.8 W/cm^2 with the four-layer emitter, which corresponds to a power density improvement of 37% with respect to the single-emitter case at the same temperature. Similarly, at the higher temperature of T_H = 2200 K, the power density reaches 666 W/cm^2, corresponding to nearly 62% improvement with respect to the single-layer emitter at the same temperature. For all considered emitters in Figure 3a,b, the power density increases as a function of emitter temperature, as expected for TPV systems.

In terms of efficiency, the reported values of maximum efficiency in Figure 3c,d for each case were determined by sweeping the load voltage from 0 to V_{oc}. Due to the presence of below-band gap absorption in InAs, the load voltage at which maximum efficiency is achieved is slightly smaller than V_{oc} (see eq 10). From Figure 3d, we see that the four-layer emitter with ω_{p2} = 0.5 eV yields a conversion efficiency of 50% at 1300 K, corresponding to a 5% improvement with respect to the single-layer case, due to a broader normalized emission bandwidth. Similarly, at T_H = 2200 K, the efficiency with the four-layer emitter with ω_{p2} = 0.5 eV reaches 53.3%, providing a nearly 13% improvement with respect to the single-layer emitter. We note that, for the temperature range T_H < 1800 K, the bilayer and four-layer cases with ω_{p2} = 0.65 eV (blue and dashed cyan curves) are suboptimal in terms of efficiency, yielding efficiencies smaller than that with the single-layer emitter, as shown in Figure 3c. In this range of temperatures with a larger ω_{p2}, the bandwidth broadening provided by the additional emitter layers is not fully exploitable due to the misalignment between the range where there is a significant photon number in the Planck distribution and $\Phi(\omega)$. Particularly, the Planck distribution is red-shifted with regard to the plasmonic resonance of the emitter near ω_{p2}. The selection of ω_{p2} should be made according to the targeted emitter temperature.

As can be seen in Figure 3c,d, the efficiency increases rapidly as a function of temperature for small emitter temperatures, while saturating at approximately 45−50% for higher temperatures, and reduces at very high temperatures outside the range displayed in Figure 3d.[30] This can be understood as follows. For $kT_H < \omega_g$, the frequency range in which the Planck distribution contains a photon number that is significantly above zero lies at energies smaller than the peak of the normalized emission spectrum, $\Phi(\omega)$. Hence, the amount of thermal photon flux received by the cell (see eq 5) is not optimized to energies around its band gap; therefore, the cell underperforms. As T_H increases, the alignment between $n(\omega, T)$ and $\Phi(\omega)$ improves, and less photonic flux is required for the cell to generate electrical power; therefore, the efficiency increases, up to the point at which the frequency range where $n(\omega, T)$ is significantly above zero extends to energies much larger than the band gap, for which its misalignment with $\Phi(\omega)$ leads to efficiency decrease, at $T_H \gg 2200$ K.

In the TPV system as considered above, the below-band-gap absorption, which is parasitic, plays an important role in determining performance. Fundamentally, below-band-gap heat exchange can be completely suppressed with the use of nonpolar semiconductors.[29] Nevertheless, this restricts the range of available band gaps and suitable emitter temperatures for TPV systems. In contrast, all polar materials exhibit below-band-gap absorption concentrated near their Reststrahlen band.[47,48] In this band, surface phonon polariton modes parasitically contribute to near-field heat transfer, leading to

https://dx.doi.org/10.1021/acs.nanolett.9b04762
Nano Lett. 2020, 20, 1654−1661

efficiency reduction in near-field TPVs.[29] For InAs, the Reststrahlen band lies at 30 meV. In the results of Figures 2 and 3, the effect of below-band gap absorption in InAs has been taken into account, and it can have a significant impact on the performance of the near-field TPV systems that we consider. For example, by calculating the ratio of below-band gap heat exchange, $P_{\omega<\omega_g}$, to the total photonic power exchange, P_{phot}, at $V = V_{oc}$ (see eq 4), we show in Figure 4a that, for the single-layer emitter configuration, below-band gap absorption constitutes nearly 60% of the total heat flux at low emitter temperatures, as shown for T_H = 500 K.

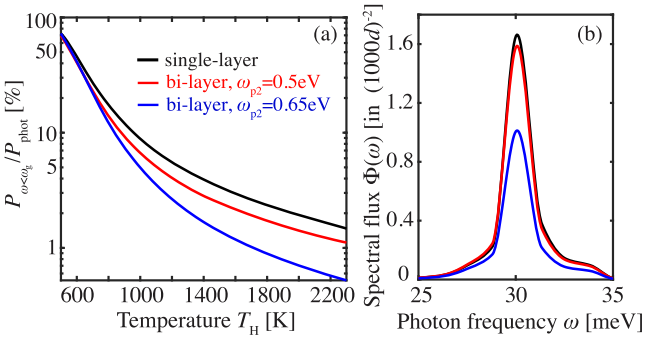

Figure 4. (a) Fraction of below-band-gap heat exchange for the same results as those in Figure 3 for an applied bias of $V = V_{oc}$. (b) Below-band gap normalized emission spectrum, $\Phi(\omega)$, near the Reststrahlen band of InAs. The black curve corresponds to the single-layer emitter case, while the blue and red ones correspond to the bilayer emitter with ω_{p2} = 0.5 and 0.65 eV, respectively.

Nevertheless, we show in Figure 4 that below-band-gap heat exchange is considerably reduced at all emitter temperatures, even for polar semiconductors like InAs, with the proposed bilayer TPV emitters considered in Figure 3. In Figure 4b, we compute the below-band-gap normalized emission spectrum, $\Phi(\omega)$, near the Reststrahlen band of InAs. It can be seen that below-band-gap photon flux is reduced in amplitude for the bilayer emitters compared to the single-layer emitter. The flux further reduces as ω_{p2} increases from ω_{p2} = 0.5 eV (red curve) to ω_{p2} = 0.65 eV (blue curve). In this range of frequencies, heat transfer is dominated by the coupling between the surface phonon polariton mode of the InAs cell and the plasmonic mode of the ITO layer closest to the vacuum gap. At a given wavevector β, the strongest coupling occurs when the two modes have similar frequencies. Consequently, we expect maximum coupling for equal dielectric permittivity between the cell and the ITO layer closest to the vacuum gap. The permittivity of InAs at 30 meV is nearly −18. For ω_{p1} = 0.44 eV (black curve), the real part of the dielectric permittivity of ITO at 30 meV is approximately −30, whereas, for the bilayer emitter with ω_{p2} = 0.5 eV (red curve), it is approximately −90 and reduces further to −150 for ω_{p2} = 0.65 eV (blue curve). Therefore, the coupling between the emitter and the cell weakens with the use of a bilayer emitter and as we increase ω_{p2}. For example, for ω_{p2} = 0.65 eV, it can be seen in Figure 4a that below-band-gap absorption can be as small as 2% and 0.57% of the total power exchange, at T_H = 1300 K and T_H = 2200 K, respectively. The overall reduction of below-band-gap heat flux in Figure 4 contributes to the large efficiency values for the bilayer emitters shown in Figure 3.

The fraction of below-band gap absorption decreases with emitter temperature, as shown in Figure 4a for all emitter cases. This can be understood, since the spectrum of the Planck distribution, $n(\omega, T_H)$, blueshifts with temperature. In contrast, the below-band gap peak of the normalized emission, $\Phi(\omega)$, shown in Figure 4b, is fixed at the Reststrahlen band of InAs. Hence, the spectral overlap between these two functions decreases with increasing emitter temperature, yielding a reduced integrated photonic heat flux below the band gap, $Q_{e,\omega<\omega_g}$ (eq 4), thereby reducing the overall heat transfer at frequencies below the band gap.

In the above results, the vacuum gap that separates the emitter from the cell was set to d = 10 nm. Nevertheless, significant practical challenges remain to be addressed in achieving such small vacuum gap sizes across parallel plates maintained at a large temperature difference in an experimental setting. Currently, the smallest practically achieved vacuum gap size reported in the TPV literature is 60 nm.[17] Hence, to account for more realistic vacuum gap sizes, next, we study the dependence of the efficiency and power density of the TPV systems considered here as the vacuum gap d ranges from 10 to 100 nm. Similar to Figure 2, we compare the single-layer emitter case with ω_{p1} = 0.44 eV, with the bilayer emitter with ω_{p2} = 0.5 eV, and the four-layer emitter with ω_{p3} = 0.6 eV and ω_{p4} = 0.575 eV, for T_H = 1300 K. As can be seen in Figure 5,

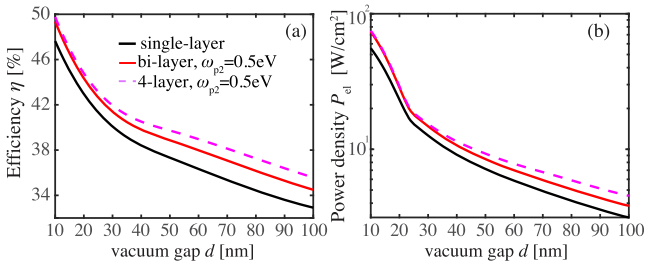

Figure 5. (a) Efficiency and (b) power density as a function of the vacuum gap size for the single-layer emitter case with ω_{p1} = 0.44 eV, the bilayer case with ω_{p2} = 0.5 eV, and the four-layer case with ω_{p3} = 0.6 eV and ω_{p4} = 0.575 eV, as in Figure 2.

both efficiency and power density decrease for increasing vacuum gap size, as expected since the radiative heat transfer between two objects in the near-field scales as $1/d^3$.[24] Nevertheless, the concept of broadening the near-field emission spectrum continues to improve the performance at larger vacuum gap sizes, in terms of both efficiency (Figure 5a) and power density (Figure 5b), as can be seen with the bilayer emitter and four-layer emitter cases. In fact, the performance improvement with respect to the single-layer emitter case increases as d increases. For example, at d = 50 nm, the improvement of the four-layer emitter case with respect to the single-layer emitter is 6.5% in terms of efficiency and 31% in terms of power density. By increasing the vacuum gap size to d = 100 nm, these improvements increase to 8 and 45% in terms of conversion efficiency and power density, respectively.

In conclusion, we have shown that broadening the normalized emission spectrum in TPV systems can lead to a simultaneous increase in the short-circuit current and open-circuit voltage in the presence of considerable nonradiative recombination. In turn, this leads to a simultaneous improvement in power density and efficiency. We further outlined a nanophotonic design strategy for practically broadening the near-field emission spectrum, by using a bilayer plasmonic emitter with an appropriately selected combination of plasma

https://dx.doi.org/10.1021/acs.nanolett.9b04762
Nano Lett. 2020, 20, 1654−1661

frequencies. The performance of near-field TPVs can be further increased by creating a gradient doping profile, readily achievable with thin film deposition of a single material that is carrier density-tunable. Using a realistic set of material parameters and considering nonidealities (thermalization, below-band gap absorption, and nonradiative recombination), we showed significant enhancement in the power density of near-field TPVs, with respect to the conventional single-layer emitter, in addition to efficiency increase and suppression of parasitic below-band gap absorption.

While advances in the measurement of near-field heat transfer between parallel interfaces[49] and the experimental realization of near-field TPV systems[17] have recently demonstrated the significant potential of near-field thermophotovoltaic energy conversion, substantial practical challenges remain to be resolved, especially for the scale-up of such systems. Nevertheless, rapid advancements in ever maturing MEMS instrumentation and nanofabrication technologies suggest that high-performance near-field TPV systems are well within reach.

AUTHOR INFORMATION

Corresponding Author

Shanhui Fan − *Department of Electrical Engineering, Ginzton Laboratory, Stanford University, Stanford, California 94305, United States*; Email: shanhui@stanford.edu

Authors

Georgia T. Papadakis − *Department of Electrical Engineering, Ginzton Laboratory, Stanford University, Stanford, California 94305, United States*; orcid.org/0000-0001-8107-9221

Siddharth Buddhiraju − *Department of Electrical Engineering, Ginzton Laboratory, Stanford University, Stanford, California 94305, United States*

Zhexin Zhao − *Department of Electrical Engineering, Ginzton Laboratory, Stanford University, Stanford, California 94305, United States*

Bo Zhao − *Department of Electrical Engineering, Ginzton Laboratory, Stanford University, Stanford, California 94305, United States*; orcid.org/0000-0002-3648-6183

Complete contact information is available at: https://pubs.acs.org/10.1021/acs.nanolett.9b04762

Notes

The authors declare no competing financial interest.

The computational package used for near-field heat transfer calculations can be found in ref 50.

ACKNOWLEDGMENTS

We acknowledge the support from the Department of Energy "Photonics at Thermodynamic Limits" Energy Frontier Research Center under Grant No. DE-SC0019140. G.T.P. acknowledges the TomKat Postdoctoral Fellowship in Sustainable Energy at Stanford University. We acknowledge discussions with Prof. M. Orenstein.

REFERENCES

(1) Narayanaswamy, A.; Chen, G. Surface modes for near field thermophotovoltaics. *Appl. Phys. Lett.* **2003**, *82*, 3544−3546.

(2) Laroche, M.; Carminati, R.; Greffet, J.-J. Near-field thermophotovoltaic energy conversion. *J. Appl. Phys.* **2006**, *100* (6), No. 063704.

(3) Park, K.; Basu, S.; King, W.; Zhang, Z. Performance analysis of near-field thermophotovoltaic devices considering absorption distribution. *J. Quant. Spectrosc. Radiat. Transfer* **2008**, *109* (2), 305−316. (Part of special issue: The Fifth International Symposium on Radiative Transfer.)

(4) Ilic, O.; Jablan, M.; Joannopoulos, J. D.; Celanovic, I.; Soljačić, M. Overcoming the black body limit in plasmonic and graphene near-field thermophotovoltaic systems. *Opt. Express* **2012**, *20* (S3), A366−A384.

(5) St-Gelais, R.; Bhatt, G. R.; Zhu, L.; Fan, S.; Lipson, M. Hot carrier-based near-field thermophotovoltaic energy conversion. *ACS Nano* **2017**, *11* (3), 3001−3009.

(6) Zhao, B.; Santhanam, P.; Chen, K.; Buddhiraju, S.; Fan, S. Near-field thermophotonic systems for low-grade waste-heat recovery. *Nano Lett.* **2018**, *18* (8), 5224−5230.

(7) Tervo, E.; Bagherisereshki, E.; Zhang, Z. Near-field radiative thermoelectric energy converters: a review. *Front. Energy* **2018**, *12*, 5−21.

(8) Song, B.; Fiorino, A.; Meyhofer, E.; Reddy, P. Near-field radiative thermal transport: From theory to experiment. *AIP Adv.* **2015**, *5* (5), No. 053503.

(9) Karalis, A.; Joannopoulos, J. D. Temporal coupled-mode theory model for resonant near-field thermophotovoltaics. *Appl. Phys. Lett.* **2015**, *107* (14), 141108.

(10) Ben-Abdallah, P.; Biehs, S.-A. Harvesting the electromagnetic energy confined close to a hot body. *Z. Naturforsch., A: Phys. Sci.* **2019**, *74*, 689.

(11) McSherry, S.; Burger, T.; Lenert, A. Effects of narrowband transport on near-field and far-field thermophotonic conversion. *J. Photonics Energy* **2019**, *9* (3), 1−13.

(12) Elzouka, M.; Ndao, S. Towards a near-field concentrated solar thermophotovoltaic microsystem: Part i modeling. *Sol. Energy* **2017**, *141*, 323−333.

(13) Bright, T. J.; Wang, L. P.; Zhang, Z. M. Performance of Near-Field Thermophotovoltaic Cells Enhanced With a Backside Reflector. *J. Heat Transfer* **2014**, *136* (03), No. 062701.

(14) Datas, A.; Vaillon, R. Thermionic-enhanced near-field thermophotovoltaics for medium-grade heat sources. *Appl. Phys. Lett.* **2019**, *114* (13), 133501.

(15) DiMatteo, R. S.; Greiff, P.; Finberg, S. L.; Young-Waithe, K. A.; Choy, H. K. H.; Masaki, M. M.; Fonstad, C. G. Enhanced photogeneration of carriers in a semiconductor via coupling across a nonisothermal nanoscale vacuum gap. *Appl. Phys. Lett.* **2001**, *79* (12), 1894−1896.

(16) DiMatteo, R. S.; Greiff, P.; Finberg, S. L.; Young-Waithe, K. A.; Choy, H. K. H.; Masaki, M. M.; Fonstad, C. G. Microngap thermophotovoltaics (mtpv). *AIP Conf. Proc.* **2002**, *653* (1), 232−240.

(17) Fiorino, A.; Zhu, L.; Thompson, D.; Mittapally, R.; Reddy, P.; Meyhofer, E. Nanogap near-field thermophotovoltaics. *Nat. Nanotechnol.* **2018**, *13* (9), 806−811.

(18) Molesky, S.; Jacob, Z. Ideal near-field thermophotovoltaic cells. *Phys. Rev. B: Condens. Matter Mater. Phys.* **2015**, *91*, 205435.

(19) Svetovoy, V. B.; Palasantzas, G. Graphene-on-silicon near-field thermophotovoltaic cell. *Phys. Rev. Appl.* **2014**, *2*, No. 034006.

(20) Karalis, A.; Joannopoulos, J. D. Squeezing near-field thermal emission for ultra-efficient high-power thermophotovoltaic conversion. *Sci. Rep.* **2016**, *6*, 28472.

(21) DeSutter, J.; Vaillon, R.; Francoeur, M. External luminescence and photon recycling in near-field thermophotovoltaics. *Phys. Rev. Appl.* **2017**, *8*, No. 014030.

(22) Zhao, B.; Chen, K.; Buddhiraju, S.; Bhatt, G.; Lipson, M.; Fan, S. High-performance near-field thermophotovoltaics for waste heat recovery. *Nano Energy* **2017**, *41*, 344−350.

(23) Shockley, W.; Queisser, H. J. Detailed balance limit of efficiency of pn junction solar cells. *J. Appl. Phys.* **1961**, *32* (3), 510−519.

(24) Rytov, S. M.; Erkku, H. *Theory of electric fluctuations and thermal radiation*; Electronics Research Directorate, Air Force Cambridge Research Center, Air Research and Development Command, U.S. Air Force: 1959.

(25) Polder, D.; Van Hove, M. Theory of radiative heat transfer between closely spaced bodies. *Phys. Rev. B* **1971**, *4*, 3303−3314.
(26) Shchegrov, A. V.; Joulain, K.; Carminati, R.; Greffet, J.-J. Near-field spectral effects due to electromagnetic surface excitations. *Phys. Rev. Lett.* **2000**, *85*, 1548−1551.
(27) Jones, A. C.; OCallahan, B. T.; Yang, H. U.; Raschke, M. B. The thermal near-field: Coherence, spectroscopy, heat-transfer, and optical forces. *Prog. Surf. Sci.* **2013**, *88* (4), 349−392.
(28) Basu, S.; Zhang, Z. M.; Fu, C. J. Review of near-field thermal radiation and its application to energy conversion. *Int. J. Energy Res.* **2009**, *33* (13), 1203−1232.
(29) Chen, K.; Santhanam, P.; Fan, S. Suppressing sub-bandgap phonon-polariton heat transfer in near-field thermophotovoltaic devices for waste heat recovery. *Appl. Phys. Lett.* **2015**, *107* (9), No. 091106.
(30) Harder, N.-P.; Wurfel, P. Theoretical limits of thermophotovoltaic solar energy conversion. *Semicond. Sci. Technol.* **2003**, *18*, S151−S157.
(31) Buddhiraju, S.; Santhanam, P.; Fan, S. Thermodynamic limits of energy harvesting from outgoing thermal radiation. *Proc. Natl. Acad. Sci. U. S. A.* **2018**, *115* (16), E3609−E3615.
(32) Nam, Y.; Yeng, Y. X.; Lenert, A.; Bermel, P.; Celanovic, I.; Soljačić, M.; Wang, E. N. Solar thermophotovoltaic energy conversion systems with two-dimensional tantalum photonic crystal absorbers and emitters. *Sol. Energy Mater. Sol. Cells* **2014**, *122*, 287−296.
(33) Omair, Z.; Scranton, G.; Pazos-Outón, L. M.; Xiao, T. P.; Steiner, M. A.; Ganapati, V.; Peterson, P. F.; Holzrichter, J.; Atwater, H.; Yablonovitch, E. Ultra-efficient thermophotovoltaic power conversion by band-edge spectral filtering. *Proc. Natl. Acad. Sci. U. S. A.* **2019**, *116* (31), 15356−15361.
(34) Palik, E. D. *Handbook of optical constants of solids*; Academic Press: Orlando, FL, 1985.
(35) Papadakis, G. T.; Zhao, B.; Buddhiraju, S.; Fan, S. Gate-tunable near-field heat transfer. *ACS Photonics* **2019**, *6* (3), 709−719.
(36) Vasudev, A. P.; Kang, J. H.; Park, J.; Liu, X.; Brongersma, M. L. Electro-optical modulation of a silicon waveguide with an "epsilon-near-zero" material. *Opt. Express* **2013**, *21*, 26387−26397.
(37) Jin, W.; Messina, R.; Rodriguez, A. W. Overcoming limits to near-field radiative heat transfer in uniform planar media through multilayer optimization. *Opt. Express* **2017**, *25* (13), 14746−14759.
(38) Naik, G. V.; Kim, J.; Boltasseva, A. Oxides and nitrides as alternative plasmonic materials in the optical range. *Opt. Mater. Express* **2011**, *1*, 1090−1099.
(39) Kafaie Shirmanesh, G.; Sokhoyan, R.; Pala, R. A.; Atwater, H. A. Dual-gated active metasurface at 1550 nm with wide (>300) phase tunability. *Nano Lett.* **2018**, *18* (5), 2957−2963.
(40) Lee, H. W.; Papadakis, G.; Burgos, S. P.; Chander, K.; Kriesch, A.; Pala, R.; Peschel, U.; Atwater, H. A. Nanoscale conducting oxide plasmostor. *Nano Lett.* **2014**, *14* (11), 6463−6468.
(41) Huang, Y.-W.; Lee, H. W. H.; Sokhoyan, R.; Pala, R. A.; Thyagarajan, K.; Han, S.; Tsai, D. P.; Atwater, H. A. Gate-tunable conducting oxide metasurfaces. *Nano Lett.* **2016**, *16* (9), 5319−5325.
(42) Jeong, C.; Kim, H.-S.; Chang, D.-R.; Kamisako, K. Effect on al2o3doping concentration of RF magnetron sputtered ZnO:al films for solar cell applications. *Jpn. J. Appl. Phys.* **2008**, *47*, 5656−5658.
(43) Chen, M.; Huang, J.; Yang, J.; Tang, K.; Lu, Y.; Wang, L. Effect of sputtering pressure on the properties of boron and gallium co-doped zno thin films. *MATEC Web Conf.* **2016**, *67*, 06073.
(44) Chen, K.; Xiao, T. P.; Santhanam, P.; Fan, S. High-performance near-field electroluminescent refrigeration device consisting of a gaas light emitting diode and a si photovoltaic cell. *J. Appl. Phys.* **2017**, *122* (14), 143104.
(45) Krishnamurthy, S.; Berding, M. Full-band-structure calculation of shockley-read-hall recombination rates in indium arsenide. *J. Appl. Phys.* **2001**, *90* (2), 848−851.
(46) "Waste heat recovery: Technology and opportunities in U.S. industry", U.S. Department of Energy, Industrial Technologies Program, 2008.
(47) Caldwell, J. D.; Glembocki, O. J.; Francescato, Y.; Sharac, N.; Giannini, V.; Bezares, F. J.; Long, J. P.; Owrutsky, J. C.; Vurgaftman, I.; Tischler, J. G.; Wheeler, V. D.; Bassim, N. D.; Shirey, L. M.; Kasica, R.; Maier, S. A. Low-loss, extreme subdiffraction photon confinement via silicon carbide localized surface phonon polariton resonators. *Nano Lett.* **2013**, *13* (8), 3690−3697.
(48) Papadakis, G. T.; Davoyan, A.; Yeh, P.; Atwater, H. A. Mimicking surface polaritons for unpolarized light with high-permittivity materials. *Phys. Rev. Materials* **2019**, *3*, 015202.
(49) Fiorino, A.; Thompson, D.; Zhu, L.; Song, B.; Reddy, P.; Meyhofer, E. Giant enhancement in radiative heat transfer in sub-30 nm gaps of plane parallel surfaces. *Nano Lett.* **2018**, *18* (6), 3711−3715.
(50) Chen, K.; Zhao, B.; Fan, S. Mesh: A free electromagnetic solver for far-field and near-field radiative heat transfer for layered periodic structures. *Comput. Phys. Commun.* **2018**, *231*, 163−172.

https://dx.doi.org/10.1021/acs.nanolett.9b04762
Nano Lett. 2020, 20, 1654−1661